

# Rethinking Cross-Attention for Infrared and Visible Image Fusion

Lihua Jian, Songlei Xiong, Han Yan, Xiaoguang Niu, Shaowu Wu, Di Zhang

**Abstract**—The salient information of an infrared image and the abundant texture of a visible image can be fused to obtain a comprehensive image. As can be known, the current fusion methods based on Transformer techniques for infrared and visible (IV) images have exhibited promising performance. However, the attention mechanism of the previous Transformer-based methods was prone to extract common information from source images without considering the discrepancy information, which limited fusion performance. In this paper, by reevaluating the cross-attention mechanism, we propose an alternate Transformer fusion network (ATFuse) to fuse IV images. Our ATFuse consists of one discrepancy information injection module (DIIM) and two alternate common information injection modules (ACIIM). The DIIM is designed by modifying the vanilla cross-attention mechanism, which can promote the extraction of the discrepancy information of the source images. Meanwhile, the ACIIM is devised by alternately using the vanilla cross-attention mechanism, which can fully mine common information and integrate long dependencies. Moreover, the successful training of ATFuse is facilitated by a proposed segmented pixel loss function, which provides a good trade-off for texture detail and salient structure preservation. The qualitative and quantitative results on public datasets indicate our ATFuse is effective and superior compared to other state-of-the-art methods.

**Index Terms**—Image fusion, Transformer, cross-attention, discrepancy information, segmented pixel loss.

## I. INTRODUCTION

AS the single-modality image has limited interpretation ability, it is difficult to meet the subsequent requirements for understanding real scenarios. Therefore, developing an effective image fusion (IF) technology is urgently needed to assist people in gaining a deep understanding of images or tackling advanced computer vision tasks. Furthermore, image fusion (IF) can provide enhanced quality images for various applications, such as remote sensing monitoring [1], object detection [2], [3], medical analysis [4], and even military engineering [5]. Specifically, infrared sensors can capture thermal radiation information in poor weather conditions but have low imaging resolution and lack fine details. Contrarily, the visible image has abundant texture information, which can compensate for this deficiency. Therefore, the fusion of IV images can integrate respective merits to form an informative image comprising salient target information and abundant

textual details. Recently, infrared and visible image fusion (IV-IF) has reached many satisfying achievements. The existing fusion methods can be made up of traditional methods [6] and deep learning-based ones [7].

A generally accepted classification for traditional fusion methods is multi-scale transform (MST)-based methods [8], sparse representation (SR)-based methods [9], saliency-based methods [10]–[12], optimization-based methods [13], [14], and hybrid-based methods [15], [16]. Among the traditional fusion methods, feature extraction and feature fusion are the two crucial steps, most of which are based on handcrafted techniques. However, blindly selecting complex transformations or representations for feature extraction often leads to time-consuming and information loss. Moreover, some manually designed fusion strategies may reduce final fusion performance as these fusion strategies are not optimized for the corresponding generated features.

Compared to traditional methods, recent advancements in deep learning have demonstrated superior computational efficiency and generalization. Existing proposed deep learning-based fusion methods are frequently implemented by leveraging either the convolutional neural network (CNN) techniques or Transformer techniques. Additionally, CNN-based methods can be further categorized into Autoencoder (AE)-based [17]–[19], end-to-end CNN-based [20]–[24], and GAN-based methods [25]–[28].

The AE-based approaches implement feature extraction and feature reconstruction through an encoder-decoder architecture, which needs to be trained in advance. However, as the handcrafted fusion strategies are not always compatible with deep extracted features, they inevitably hinder the improvement of fusion performance. Therefore, the end-to-end CNN-based approaches are introduced to directly generate the fused image under the specified constraints of a well-defined loss function. The GAN-based methods employ a min-max optimization game between generators and discriminators to solve the image fusion problem. Specifically, the generator is used to produce fusion results that closely match the distributions of the source image, and it can even deceive the discriminator. However, these CNN-based methods containing convolution operations can merely explore local information using fixed kernel size but lack consideration of the global information of an image.

By contrast, the Transformer is equipped with self-attention and cross-attention mechanisms, which can effectively extract long-range context information and has exhibited excellent performance in many vision tasks apart from natural language processing [29]–[32]. Recently, Transformer-based architec-

Lihua Jian, Songlei Xiong, Han Yan and Di Zhang are with the School of Electrical and Information Engineering, Zhengzhou University, Zhengzhou, Henan, 450001 P.R.China (e-mail: ielhjian@zzu.edu.cn; xsl@gs.zzu.edu.cn; han\_yan0714@gs.zzu.edu.cn; dr.di.zhang@ieee.org).

Xiaoguang Niu and Shaowu Wu are with the School of Computer Science, Wuhan University, Wuhan, Hubei, 430072, P.R.China (e-mail: xg-niu@whu.edu.cn; wshaow@whu.edu.cn).

ture has been introduced into the image fusion community [33]–[37]. These attempts have demonstrated long-range dependence, extracted by the self-attention mechanism and cross-attention mechanism, can further improve the quality of fusion outcomes [38], [39].

Despite the comparable results achieved by existing Transformer-based fusion, several challenges still exist in this domain. First, the attention mechanism is only used to capture common information of source images, while the discrepancy information has not been effectively separated and utilized. Second, a single Transformer module can not completely extract common information. The aforementioned issues significantly reduce fusion efficiency. Third, the existing pixel loss functions typically adopt a fixed approach, i.e., pixel maximum or weighted average, to guide the fusion process, which does not effectively preserve complete information.

To address the above-mentioned drawbacks, we devise an alternate Transformer fusion network (ATFuse) based on a modified cross-attention mechanism. For capturing the discrepancy information from two source images, we modify the cross-attention mechanism and propose a discrepancy information injection module (DIIM). To fully extract common information and integrate long dependencies of the source images, we design an alternate common information injection module (ACIIM). In addition, we propose a segmented pixel loss function that utilizes different constraints on pixel values to guide the fusion network. This proposed loss function can ensure the preservation of intensity information in fused images adequately.

The main contributions of this paper are summarized as follows:

- An end-to-end ATFuse network is proposed for the fusion of IV images. Extensive experiments on multiple datasets show that our proposed ATFuse method achieves good effect and generalization ability.
- A discrepancy information injection module (DIIM) is proposed based on the cross-attention mechanism. With this DIIM, the unique features of the source images can be explored respectively.
- An alternate common information injection module (ACIIM) is applied to the proposed framework, in which common information is fully retained in the final result.
- A segmented pixel loss function composed of different pixel intensity constraints is designed to train ATFuse so that the preservation of texture details and brightness information can reach a good trade-off in the fused results.

The structure of this paper is as follows. Section II surveys the related work. Section III states the proposed ATFuse framework. Section IV presents the experimental analysis and discussion. Section V summarizes this paper.

## II. RELATED WORK

In this section, we review the current CNN-based and Transformer-based IV-IF methods.

### A. CNN-based Image Fusion Methods

Deep learning (DL) has been widely introduced into computer vision tasks such as image restoration [40], person re-identification [41], [42], and image super-resolution [43]. Attributed to the superior feature representation ability, DL-based IV-IF methods also have occupied the leading position in recent years. CNN was initially introduced into the field of IF by Liu et al. [44], using Siamese convolutional networks to generate weight maps. Li et al. [17] proposed a dense-connection AE-based approach, DenseFuse, to fuse IV images, avoiding information loss of deep features in the fused results. Jian et al. [19] designed an attention mechanism to fuse deep features based on a symmetric AE network, which enhanced the salient information of infrared images in the fused results. Li et al. [18] trained a learnable fusion network at two stages to further preserve image details and overcome the limitations of hand-crafted fusion strategies. Similarly, Ma et al. [45] proposed an end-to-end model that utilized a salient target mask to guide the network training to highlight the thermal information. To improve the model generalization, Xu et al. [24] developed a unified unsupervised fusion framework to deal with different fusion tasks.

Most GAN-based fusion methods use an unsupervised manner to force the distribution of the fused result approach distributions of source images by a specific loss function. As a key milestone, Ma et al [25] first applied GAN to IV-IF. After that, various GAN-based variants have been proposed to boost the fusion performance. For example, Li et al. [46] utilized the coupled generative adversarial network for the image fusion task. Ma et al. [47] designed a DDcGAN, in which the high- and low-version of the fused image produced by a generator were used to deceive two discriminators respectively, to achieve the preservation of infrared information and detail information. To prevent the fused image from being biased to one of the source images, Ma et al. [48] adopted multiclassification constraints to achieve information balance.

### B. Transformer-based Fusion Methods

Transformer was first proposed by Vaswani et al. [29] to address natural language processing issues and achieved remarkable success. Subsequently, Dosovitskiy et al. [49] designed visual Transformers to conduct an image classification task. Due to its self-attention mechanism that can capture long-range dependencies, the Transformer has been applied to many computer vision tasks, such as target detection [50]–[52], video inpainting [53]–[55], and image super-resolution [56]–[58]. In recent, some Transformer-based methods have been presented to handle IV-IF [59]–[62].

Vs et al. [34] utilized a spatial branch and a Transformer branch fusion strategies to merge local and global information, respectively. Wang et al. [63] proposed a residual Swin Transformer to extract the global features that further enhanced the representation ability of the previous Transformer in IV-IF tasks. In a similar manner, Ma et al. [39] integrated cross-domain learning with Swin Transformer to fully use the inter- and intra-domain contexts for fusion. To overcome hand-crafted fusion rules existing in Transformer-based fusion

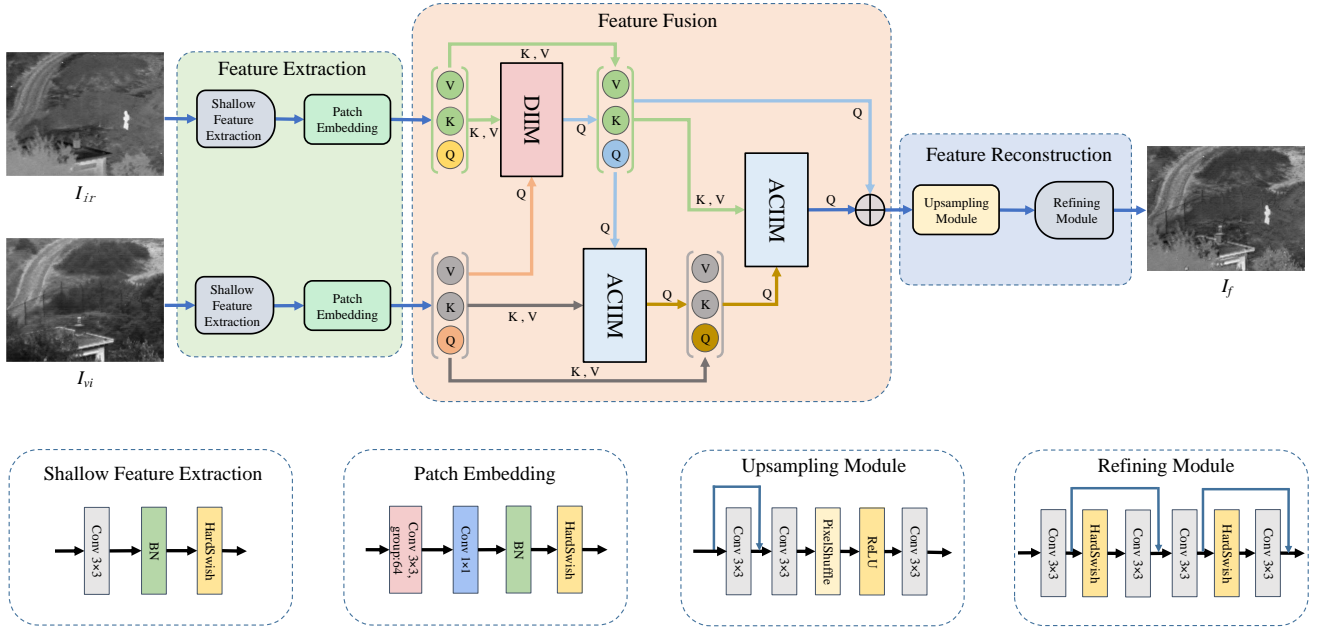


Fig. 1. The overall framework of ATFuse.

models, Tang et al. [37] proposed an end-to-end Transformer architecture to fuse IV images.

Upon reviewing the previous Transformer-based fusion methods, we discovered certain limitations and rethought the usage of the cross-attention mechanism. Most studies based on Transformer structure merely grasp the global information of an image, aiming to compensate for the drawbacks of convolutional operations only capturing local information. To the best of our knowledge, both self-attention and cross-attention do not consider the discrepancy information between multimodalities in the application of IV-IF. Additionally, to fully exploit common information and long-range dependencies of source images, we adopt an alternating extraction approach depending on the original cross-attention mechanism.

### III. METHODOLOGY

In this section, the overall framework of our proposed ATFuse is first introduced in Section III-A. Subsequently, in Section III-B, two modified cross-attention modules, DIIM and ACIIM, specifically designed for image fusion tasks are described. Finally, the loss function in our work is presented in Section III-C.

#### A. Framework Overview

As illustrated in Fig. 1, the overall architecture of our ATFuse consists of a feature extraction module, a feature fusion module, and a feature reconstruction module. First, the source IV images are fed into the feature extraction module to extract shallow features and then transform them into patch embedding. Afterward, a feature fusion module is established for fusing discrepancy features and common features. Finally, a feature reconstruction is utilized to map the fused features into a composite image. Here we briefly introduce the proposed architecture.

*Feature extraction.* Since the convolutional layers have stability and enhanced optimization ability [64], a convolutional layer with a kernel size of  $3 \times 3$  is still used to extract shallow local features in the feature extraction module. After that, there is a batch normalization (BN) layer and a HardSwish activation function. The feature extraction process can be formulated as:

$$\{F_{ir}^{sf}, F_{vi}^{sf}\} = \{SF(I_{ir}), SF(I_{vi})\}, \quad (1)$$

where  $I_{ir}$  and  $I_{vi}$  are source images.  $F_{ir}^{sf}$  and  $F_{vi}^{sf}$  denote the output features of shallow feature extraction  $SF(\cdot)$ . Subsequently, we use the patch embedding module  $PE(\cdot)$  to transform the feature maps  $F_{ir}^{sf}$  and  $F_{vi}^{sf}$  to yield a series of token sequences  $F_{ir}^{token}$  and  $F_{vi}^{token}$ , respectively. Then these tokens are fed to the subsequent DIIM and ACIIM. The process of the patch embedding can be expressed as:

$$\{F_{ir}^{token}, F_{vi}^{token}\} = \{PE(F_{ir}^{sf}), PE(F_{vi}^{sf})\}. \quad (2)$$

*Feature fusion.* The  $F_{ir}^{token}$  and  $F_{vi}^{token}$  are fed to feature fusion module  $FF(\cdot)$  to generate the fused feature  $F_f$ . The feature fusion process can be formulated as:

$$F_f = FF(F_{ir}^{token}, F_{vi}^{token}), \quad (3)$$

where  $FF(\cdot)$  contains a DIIM ( $DIIM(\cdot)$ ) and a pair of ACIIMs ( $ACIIM(\cdot)$ ), which are designed to further extract global dependencies features, i.e., discrepancy features and common features, respectively. It can be represented as:

$$\begin{aligned} Z_1 &= DIIM(F_{ir}^{token}, F_{vi}^{token}), \\ Z_2 &= ACIIM(F_{vi}^{token}, Z_1), \\ Z_3 &= ACIIM(F_{ir}^{token}, Z_2), \\ FF(F_{ir}^{token}, F_{vi}^{token}) &= Z_3 + Z_1, \end{aligned} \quad (4)$$

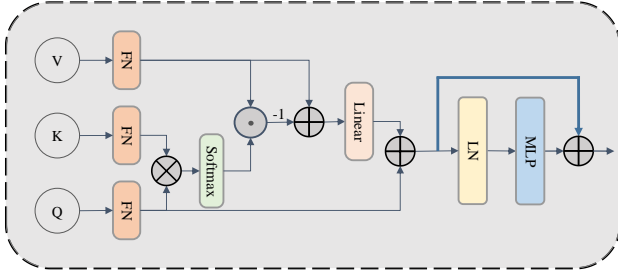


Fig. 2. The architecture of discrepancy information injection module (DIIM).

where  $Z_1$ ,  $Z_2$ , and  $Z_3$  are the outputs of DIIM, the first ACIIM, and the second ACIIM respectively. A detailed description of DIIM and ACIIM is provided in Section 3.2.

*Feature reconstruction.* The fused feature  $F_f$  is fed into an upsampling module  $UP(\cdot)$  to resize back to the source images. Besides, we use the residual network-based refining module  $RE(\cdot)$  to further recover the detail information of the fused image  $I_f$ . The feature reconstruction process can be expressed as:

$$I_f = RE(UP(F_f)). \quad (5)$$

### B. DIIM and ACIIM.

The goal of IV-IF is to obtain a comprehensive image that contains salient targets while preserving rich textural details. Thus, how to fully exploit discrepancy and common information present in the source images is a key determinant of the fusion performance. Motivated by the argument that the cross-attention mechanism is effective in extracting common features among images, we propose DIIM and ACIIM.

To effectively obtain the discrepancy features between infrared and visible image features produced by the previous stage, we use a newly built cross-attention architecture, as illustrated in Fig. 2. It is given the  $F_{ir}^{token}$  and  $F_{vi}^{token}$  as input and the discrepancy information features as output. Specifically, to explore the long-range relationship of IV features, we partition the  $F_{ir}^{token}$  and  $F_{vi}^{token}$  into  $s$  local feature segments as:

$$\begin{aligned} Q_1, \dots, Q_s &= Partition(F_{vi}^{token}), \\ K_1, \dots, K_s &= Partition(F_{ir}^{token}), \\ V_1, \dots, V_s &= Partition(F_{ir}^{token}), \end{aligned} \quad (6)$$

where  $F_{vi}^{token}$  and  $F_{ir}^{token} \in \mathbb{R}^{h \times w \times c}$ , and  $s = h \times w$ . Afterward, we employ the linear layer to transform the token segments into the query  $Q$ , key  $K$ , and value  $V$ , which are three fundamental elements of the base Transformer. The linear projection can be expressed as:

$$\begin{aligned} Q_i &= Linear_Q(Q_i), \\ K_i &= Linear_K(K_i), \\ V_i &= Linear_V(V_i), \end{aligned} \quad (7)$$

where  $i = 1, \dots, s$ , the  $Linear(\cdot)$  is a linear projection operator that is shared across different segments.

To explore the common information of infrared and visible image features with the consideration of long-term relationships, we use the dot-product attention layer to compute the similarity matrix between  $Q_i$  and  $K_j$  ( $i$  and  $j$  belong to 1 through  $s$ ), and then multiply by the  $V$  to infer the common information between  $Q$  and  $V$ . This process can be expressed as:

$$CM_{QV} = softmax\left(\frac{Q_{1,\dots,s}K_{1,\dots,s}^T}{\sqrt{d_k}}\right)V, \quad (8)$$

where  $d_k$  is a scaling factor, which can alleviate the softmax function from converging to regions of minimal gradients as the dot product increases. Subsequently, we can easily obtain the discrepancy information between  $Q$  and  $V$  by removing the common information. This process can be represented as:

$$DIM_{QV} = Linear(V - CM_{QV}). \quad (9)$$

To obtain complementary information from the IV images, we inject the discrepancy information into  $Q$ , which can be formulated as:

$$\begin{aligned} F_{add} &= DIM_{QV} + Q \\ F_{diim} &= MLP(LN(F_{add})) + F_{add}, \end{aligned} \quad (10)$$

where  $LN(\cdot)$  represents layer normalization,  $MLP(\cdot)$  represents multi-layer perceptron and  $F_{diim}$  is the output of the DIIM.

To illustrate the effectiveness of the modified cross-attention, we compare the feature maps generated by the DIIM with those generated by the vanilla cross-attention. The results are shown in Fig. 4. The feature maps illustrate that the information injection module utilizing the vanilla cross-attention mechanism can solely incorporate common information from both images, lacking the capability to integrate discrepancy information across different modalities. Consequently, the resultant output feature maps predominantly encompass information from one image, while lacking modality-specific details from the other image, making them unsuitable for multimodal image fusion tasks. In contrast, our DIIM significantly compensates for this deficiency.

As depicted in Fig. 3, although the obtained feature maps generated by the DIIM almost contain all the salient edge information, the background detail information is not completely preserved in the fusion features. Thus, it is essential to further enhance the fused features by incorporating common information from both the IV images. Following the DIIM, the proposed ATFuse alternately extracts common information reflecting the background details from the IV images through the ACIIM module. The structure of ACIIM is illustrated in Fig. 4. We first inject common information from visible images to enrich the fused information. Specifically, given that the segments of  $F_{diim}$  are used as  $Q_{1,\dots,s}$  and the segments of  $F_{vi}^{token}$  are used as  $K_{1,\dots,s}$  and  $V_{1,\dots,s}$ , the common information between  $F_{diim}$  and  $F_{vi}^{token}$  can be expressed as:

$$CM_{vi}^{token} = softmax\left(\frac{Q_{1,\dots,s}K_{1,\dots,s}^T}{\sqrt{d_k}}\right)V. \quad (11)$$

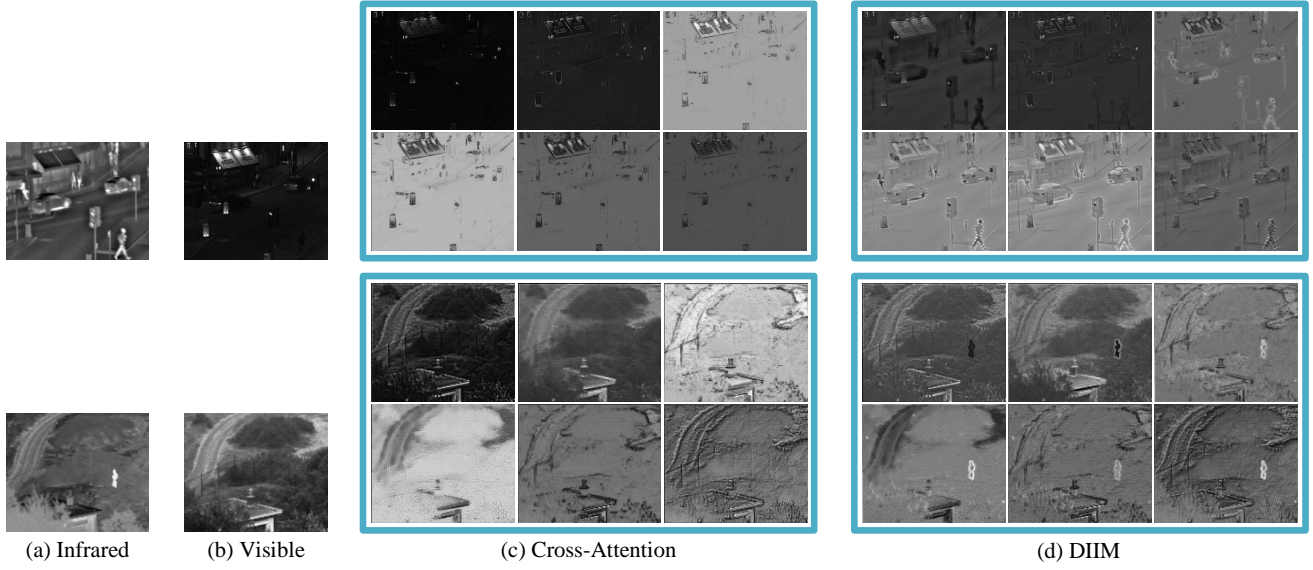


Fig. 3. Partial feature maps obtained from the two different modules. (a) infrared image, (b) visible image, (c) partial features obtained by the vanilla cross-attention, (d) partial features obtained by the DIIM.

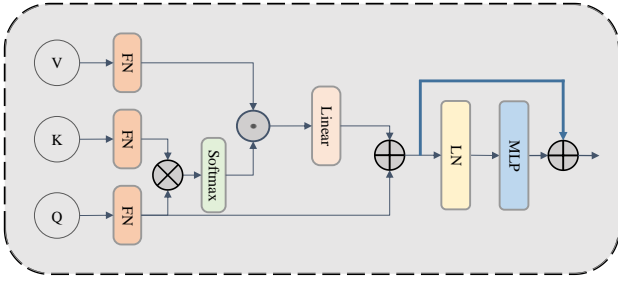


Fig. 4. The architecture of alternate common information injection module (ACIIM).

Then, the common information  $CM_{vi}^{token}$  between  $F_{diim}$  and  $F_{vi}^{token}$  is added with  $F_{diim}$ . The process can be formulated as:

$$\begin{aligned} F_{add} &= Linear(CM_{vi}^{token}) + Q, \\ F_{acim}^{vi} &= MLP(LN(F_{add})) + F_{add}, \end{aligned} \quad (12)$$

where  $F_{acim}^{vi}$  represents the output of the first ACIIM.

Afterward, the common information between  $F_{acim}^{vi}$  and  $F_{ir}^{token}$  should also be injected into the fused features to enrich the fused features. This process follows the same manner as above Eq. 12.

### C. Loss Function

Since the proposed ATFuse is trained in an unsupervised end-to-end manner, the choice of loss function greatly affects the fusion performance. Considering the different imaging mechanisms of IV images, the loss function of the proposed method makes sure that the fusion results can preserve sufficient details and salient information. The loss function of our ATFuse can be defined as:

$$\mathcal{L} = \mathcal{L}_{pixel} + \gamma \cdot \mathcal{L}_{texture}, \quad (13)$$

where  $L_{pixel}$  and  $L_{texture}$  represent the pixel loss and texture loss, respectively.  $\gamma$  is a hyperparameter to balance these two loss terms.

Motivated by [65], the texture detail of an image can be represented by maximum aggregation around the gradients. Thus, the texture loss is designed to regulate the gradients in the fused image as follows:

$$\mathcal{L}_{texture} = \frac{1}{HW} \|\nabla I_f - \max\{\nabla I_{ir}, \nabla I_{vi}\}\|_1, \quad (14)$$

where  $\nabla$  represents the Sobel operator, which is used to calculate the gradient.  $\|\cdot\|_1$  represents the  $l_1$ -norm.  $H$  and  $W$  denote height and width respectively.  $\max\{\cdot\}$  represents the element-wise maximum selection.

It is known that maximum value selection-based pixel loss weakens the importance of pixels in one of the source images, while the average pixel loss may reduce the saliency of fusion results. Therefore, to achieve a better compromise between the preservation of important information and the enhancement of salient information, we adopt a segmented pixel loss function to train the proposed framework. In this work, the importance of a pixel is defined as the product of the pixel value and its gradient value as

$$pi = \nabla I \cdot I, \quad (15)$$

where  $I$  represents the pixel value, while  $\nabla I$  denotes the corresponding gradient value.

The importance of each pixel in the two source images is assessed and categorized into two segments as follows,

$$\begin{aligned} p_{part1} &= \{p | (pi \geq pi_{ir}^\alpha \text{ or } pi \geq pi_{vi}^\alpha)\}, \\ p_{part2} &= \{p | (pi < pi_{ir}^\alpha \text{ and } pi < pi_{vi}^\alpha)\}, \end{aligned} \quad (16)$$

where  $pi_{vi}^\alpha$  and  $pi_{ir}^\alpha$  represent the top  $\alpha\%$  important pixels.  $p_{part1}$  denotes the first segment that consists of the most crucial pixels covering the top  $\alpha\%$  important pixels from each

source image. The remaining pixels are represented as the second segment  $p_{part2}$ .

As depicted above, we apply different pixel loss functions to each segment to meet the tradeoff among pixels of different importance. The maximum value selection-based pixel loss is employed in  $p_{part1}$ , which can emphasize the saliency of these pixels in the fused image. Meanwhile, for  $p_{part2}$ , we use the pixel average loss to force the fused image to approximate each source image. The segmented pixel loss can be formulated as follows:

$$\begin{aligned}\mathcal{L}_{part1} &= \frac{1}{HW} \|I_f - \max(I_{ir}, I_{vi})\|_1, \quad p \in p_{part1}, \\ \mathcal{L}_{part2} &= \frac{1}{2HW} (\|I_f - I_{ir}\|_1 + \|I_f - I_{vi}\|_1), \quad p \in p_{part2},\end{aligned}\quad (17)$$

where  $I_{ir}, I_{vi}$  are source images.  $I_f$  is the fused image. The final pixel loss function can be rewritten as follows.

$$\mathcal{L}_{pixel} = \mathcal{L}_{part1} + \mathcal{L}_{part2}, \quad (18)$$

#### IV. EXPERIMENTS

In this section, we first introduce the datasets and implementation settings. Then, the comparative experimental methods and objective evaluation metrics are described. After that, the experiment results and discussion are reported. Furthermore, we conduct the ablation experiments and present the analysis of some hyperparameters and computational efficiency.

##### A. Datasets and Implementation Settings

In this study, we utilize the recent publicity datasets RoadScene [24] and MSRS [65], in which we select 201 pairs of IV images from each dataset. Then, these images are randomly cropped into sample patches with the size of  $128 \times 128$  for training. To train the proposed ATFuse, we utilize the AdamW optimizer to update the network parameters with an initial learning rate of  $2 \times 10^{-3}$ , which is decreased by 50% each time after 50, 100, 200, and 400 epochs. The batch size is set to 16. The parameters  $\alpha$  and  $\gamma$  are set to 20 and 1.0, respectively. The configurations for all experiments are computed with an NVIDIA GeForce RTX 4090 GPU and 64 GB RAM. The framework is programmed on PyTorch.

##### B. Comparative Methods and Objective Evaluation Metrics

*Comparative Methods:* To assess the superiority of our method, we select six state-of-the-art image fusion methods for comparison, including two Transformer-based methods: DATFuse [37] and SwinFusion [39], two autoencoder-based methods: DenseFuse [17] and RFN-Nest [18], an end-to-end CNN-based method: U2Fusion [24], and a GAN-based method: FusionGAN [25]. The source codes of all compared methods are publicly available and all parameters are configured as suggested in the original papers.

*Objective Evaluation Metrics:* Six objective evaluation metrics are chosen to quantitatively evaluate the performance of all methods: Average gradient ( $AG$ ), Entropy ( $EN$ ) [66], Standard deviation ( $SD$ ) [67], Spatial frequency ( $SF$ ) [68], Visual

information fidelity ( $VIFF$ ) [69] and  $Q_{abf}$ .  $AG$  measures the sharpness or clarity of an image.  $EN$  is an objective measure of the amount of information contained in an image.  $SD$  is a statistical theory-based standard deviation that reflects the degree of change in pixel brightness.  $SF$  is a measure based on gradient distribution, which represents the rate of change of the grayscale of the fused image.  $VIFF$  measures the quality of the fusion image according to visual information fidelity.  $Q_{abf}$  is a non-reference quality evaluation index by estimating the degree of salient information from source images represented in the fused image. Higher values of these metrics correspond to better quality of the fused image.

##### C. Results and Discussion

1) *Results on RoadScene Dataset:* Fig. 5 shows five pairs of source infrared and visible images from the RoadScene dataset along with fusion results obtained through seven methods. Two localized areas in each image are magnified for better comparison. It is apparent that all seven methods can perform relatively good fusion effects. However, the other six methods still have some unsatisfactory performance. Obviously, results generated by DATFuse, SwinFusion, and ATFuse methods have more detailed information and salient information than those without using the Transformer architectures, since the attention mechanism of the Transformer can capture global information. Nevertheless, DATFuse and SwinFusion still have deficiencies when dealing with specific local information. As can be seen, the salient information of fusion results by DATFuse is relatively worse since it fails to extract distinctive information from the infrared image (see the red box in the second row and the green box in the first row). The SwinFusion method shows poor performance when processing low-saliency but information-rich regions (see the red box in the fourth row and the green box in the fifth row). One possible reason is that the pixel loss of SwinFusion makes the pixels of the fusion result completely tend to the maximum value of the source image, ignoring the information of the lower pixel values. Besides, DenseFuse, FusionGAN, RFN-Nest, and U2Fusion fail to preserve significant information from the infrared image well in the fusion results (see the green box in the first row and the red box in the second row). By contrast, it can be seen that our ATFuse maintains the salient information in all results, this is because the proposed ATFuse employs DIIM and ACIIM modules, which can generate results containing various types of information. Furthermore, the segmented pixel loss function enables our method to balance the retention of detailed information and salient information better.

Fig. 6 further reports quantitative results on the twenty image pairs of the RoadScene dataset by using six objective evaluation metrics. Results indicate that our proposed method performs the best average values on the four evaluation metrics (i.e.,  $AG$ ,  $SF$ ,  $VIFF$ , and  $Q_{abf}$ ).  $EN$  and  $SD$  rank second place as close to the best performance. Overall, our method has achieved satisfactory objective performance, which demonstrates the crucial role of the proposed network structure and the segmented pixel loss function.

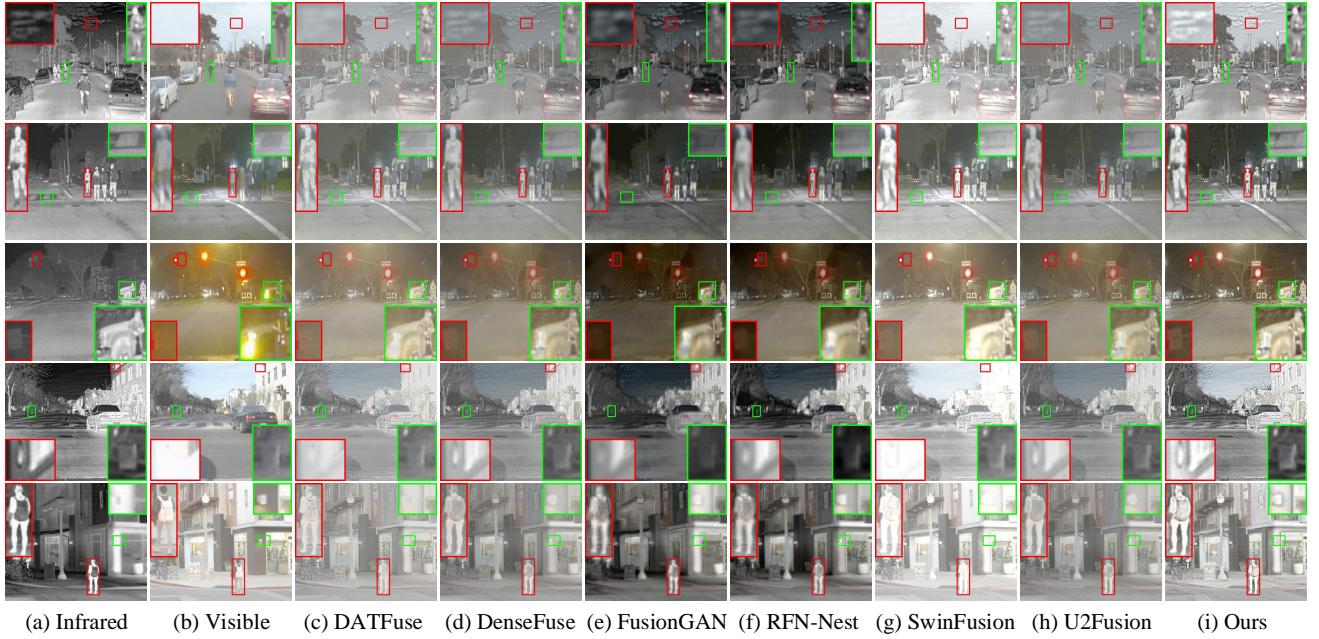


Fig. 5. Qualitative comparison of ATFuse with six state-of-the-art visible and infrared image fusion methods on the RoadScene dataset. (a) infrared image, (b) visible image, (c) DATFuse [37], (d) DenseFuse [17], (e) FusionGAN [25], (f) RFN-Nest [18], (g) SwinFusion [39], (h) U2Fusion [24], (i) Ours.

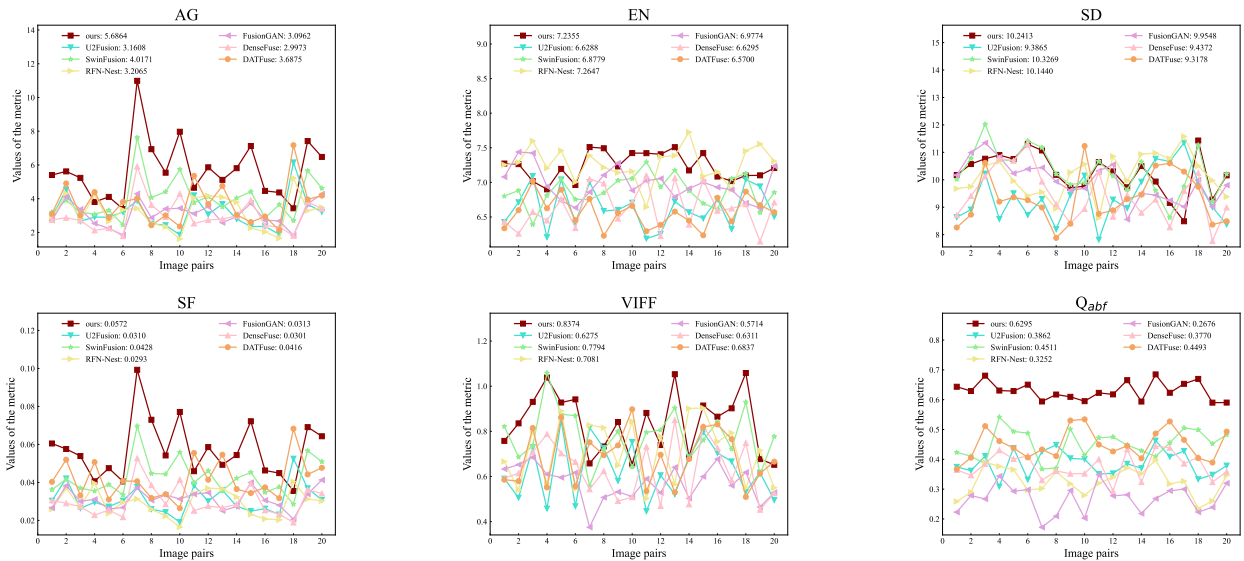


Fig. 6. Using six metrics to quantitatively compare ATFuse with six existing fusion methods on the RoadScene dataset (twenty image pairs). The average of all metrics is shown in the legend.

2) *Results on MSRS Dataset:* Fig. 7 displays the fusion results obtained by the seven comparison methods on the MSRS dataset. Although the existing fusion methods can obtain results by retaining information from the source images to some extent, they still encounter detail blurring and salient information loss. Specifically, the results generated by DATFuse lose different degrees of detail information from the visible image (see Fig. 7(c)). DenseFuse, FusionGAN, RFN-Nest, and U2Fusion fail to effectively balance the infrared information and visible information, such as the blurred effects around the tower edges in the red boxes of the last row. SwinFusion seems

to have richer details and brightness information. However, it loses some details from the infrared images, since this method utilizes a pixel maximum constraint loss for each pixel. (see the red boxes in the first and fifth rows). In contrast, our ATFuse achieves a better tradeoff between detail preservation and salient information retention.

Table I displays objective evaluations of seven different fusion methods on twenty image pairs from the MSRS dataset. Our ATFuse method performs best in the  $AG$ ,  $SF$ , and  $Q_{abf}$  metrics. The remaining three metrics are slightly different from the best ones. Specifically, our method performs second-best in

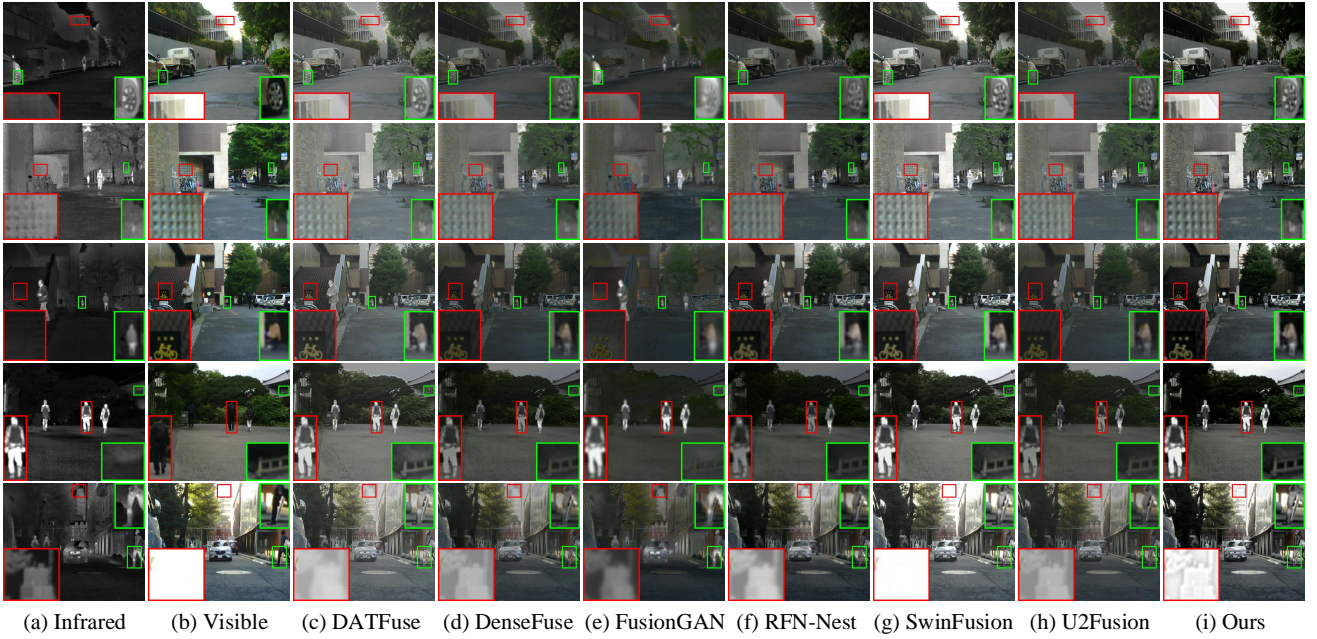


Fig. 7. Qualitative comparison of ATFuse with six state-of-the-art visible and infrared image fusion methods on the MSRS dataset. (a) infrared image, (b) visible image, (c) DATFuse [37], (d) DenseFuse [17], (e) FusionGAN [25], (f) RFN-Nest [18], (g) SwinFusion [39], (h) U2Fusion [24], (i) Ours.

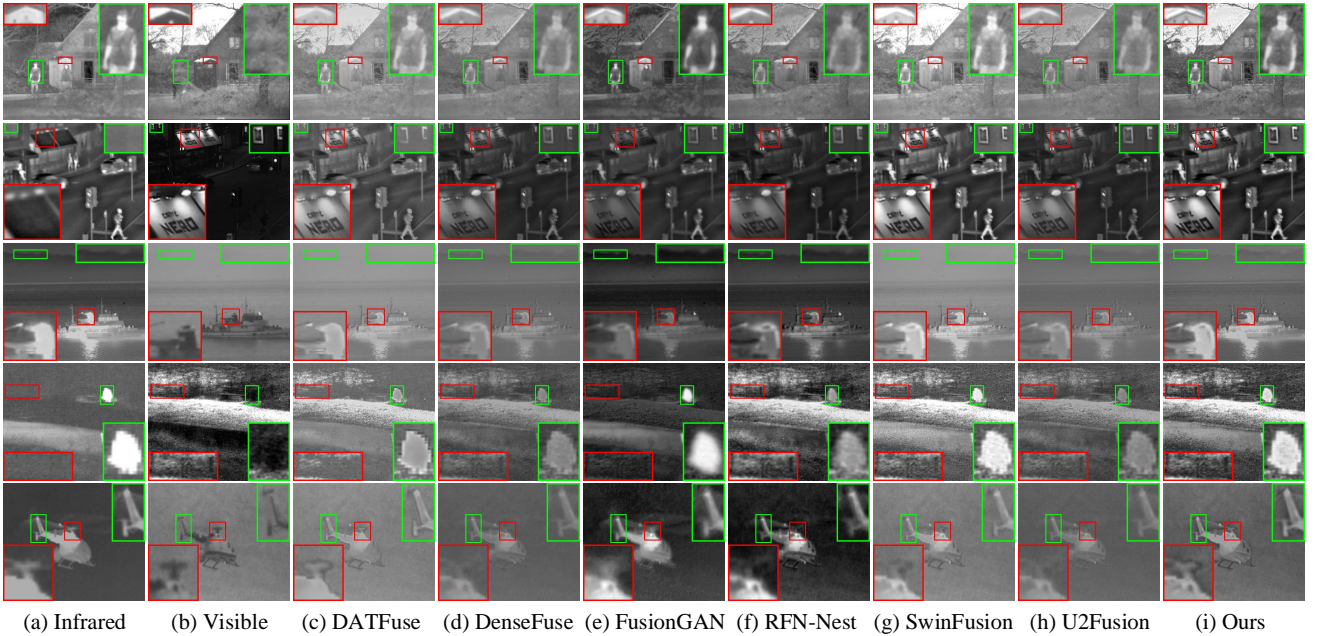


Fig. 8. Qualitative comparison of ATFuse with six state-of-the-art visible and infrared image fusion methods on the TNO dataset. (a) infrared image, (b) visible image, (c) DATFuse [37], (d) DenseFuse [17], (e) FusionGAN [25], (f) RFN-Nest [18], (g) SwinFusion [39], (h) U2Fusion [24], (i) Ours.

the *EN* and *VIFF* metrics and third-best in the *SD* metric. Overall, based on subjective and objective analysis, we can conclude that our ATFuse method achieves the best fusion performance and outperforms other methods in both visual perception and objective metrics.

3) *Extension Experiment on TNO Dataset:* To further validate the effectiveness and generalization capabilities of our method, we directly utilize the trained model to test the generalization on the TNO dataset. Fig. 8 shows five image

pairs from the TNO dataset and the corresponding fusion results obtained by seven methods. We have magnified two local areas in each image for better comparison. It can be seen that the six comparison methods still have some drawbacks compared to our method. Specifically, DenseFuse, RFN-Nest, and U2Fusion fail to extract enough salient information from the infrared images compared to the other methods (see the red box in the second row and the green box in the fourth row). Moreover, the results produced by FusionGAN are mostly

TABLE I

USING SIX METRICS TO QUANTITATIVELY COMPARE ATFUSE WITH SIX EXISTING FUSION METHODS ON THE MSRS DATASET (TWENTY IMAGE PAIRS). THE BEST AND THE SECOND BEST PERFORMANCE IS MARKED BY **BOLD** AND UNDERLINED, RESPECTIVELY.

Methods	<i>AG</i>	<i>EN</i>	<i>SD</i>	<i>SF</i>	<i>VIFF</i>	<i>Q<sub>abf</sub></i>
DATFuse	4.1944	6.8679	<b>9.3450</b>	<u>0.0529</u>	0.8020	0.5919
DenseFuse	2.5050	6.4331	8.2278	0.0284	0.7052	0.3733
FusionGAN	1.7466	5.7239	6.6471	0.0200	0.5730	0.1358
RFN-Nest	2.6218	6.6975	8.5525	0.0282	0.7499	0.4152
SwinFusion	<u>4.3921</u>	<b>7.1548</b>	<u>9.1247</u>	0.0526	<b>1.0195</b>	<u>0.6332</u>
U2Fusion	2.5714	6.3092	7.9221	0.0297	0.6607	0.3920
Ours	<b>4.6872</b>	<u>7.1441</u>	8.9113	<b>0.0551</b>	<u>0.9718</u>	<b>0.6982</b>

blurry around the edges (see the green box in the fourth row and the red box in the fifth row). For DATFuse, SwinFusion, and our method, the overall saliency in DATFuse is notably worse (see the green box in the fourth row), because it adopts an average constraint approach for each pixel in the loss function, leading to a saliency reduction of the results. SwinFusion loses some detailed information in the visible image due to its loss function making the values of all pixels in the fused image close to the maximum values of the corresponding pixels in the two source images (see the red box in the fifth row). In contrast, the proposed segmented pixel loss function makes the fused pixel values tend toward the maximum values of corresponding pixel points in target regions, resulting in better preservation of salient information. Furthermore, our method effectively extracts discrepancy information from two source images, whereas SwinFusion and DATFuse struggle to capture the distinct information of infrared images (see the green box in the third row).

TABLE II

USING SIX METRICS TO QUANTITATIVELY COMPARE ATFUSE WITH SIX EXISTING FUSION METHODS ON THE TNO DATASET (TWENTY IMAGE PAIRS). THE BEST AND THE SECOND BEST PERFORMANCE IS MARKED BY **BOLD** AND UNDERLINED, RESPECTIVELY.

Methods	<i>AG</i>	<i>EN</i>	<i>SD</i>	<i>SF</i>	<i>VIFF</i>	<i>Q<sub>abf</sub></i>
DATFuse	3.1016	6.3137	8.1289	0.0334	0.7214	0.4802
DenseFuse	2.3471	6.1386	7.9529	0.0236	0.6065	0.3435
FusionGAN	2.2010	6.3553	8.0122	0.0226	0.6515	0.2190
RFN-Nest	2.7671	<u>6.8298</u>	<b>8.7919</b>	0.0243	0.7970	0.3649
SwinFusion	<u>3.9429</u>	6.7155	8.6421	<u>0.0400</u>	<u>0.8467</u>	0.5150
U2Fusion	2.4238	6.1319	7.9008	0.0226	0.6020	0.3593
Ours	<b>4.3232</b>	<b>6.8774</b>	8.5891	<b>0.0431</b>	<b>0.8559</b>	<b>0.5900</b>

Table II reports that our method achieves the best fusion effects in *AG*, *EN*, *SF*, *VIFF*, and *Q<sub>abf</sub>* metrics on the TNO dataset. The *SD* metric record of our method is third-best, with a small difference compared to the best performance. In general, the ATFuse method achieves the best objective and subjective performance among the seven methods, testing the twenty image pairs from the TNO dataset, and affirming its excellent generalization ability.

#### D. Ablation Studies

In this section, we have conducted two ablation studies to investigate the effectiveness of our method, namely, network structures and the segmented pixel loss function.

1) *Ablation Study on Network Structure*: To investigate the effectiveness of DIIM and ACIIM, we separately remove the DIIM (named “w/o DIIM”), and the ACIIM (named “w/o ACIIM”). We compare the fusion results obtained by w/o ACIIM, w/o DIIM, and the proposed method, as shown in Fig. 9. It can be seen that fusion results produced by using w/o DIIM only contain detail information from the visible image, while the salient information from the infrared image is almost entirely lost (see the green boxes in Fig. 9(c)). Besides, our fusion results have more detail information than the results by using w/o ACIIM network (see the red boxes Fig. 9(d-e)). The main reasons lie in that the proposed ATFuse embeds the DIIM and ACIIM modules, which have a good ability to capture the discrepancy information and the common information of the source images.

TABLE III

QUANTITATIVE COMPARISON OF FUSION RESULTS OBTAINED BY THREE DIFFERENT NETWORK STRUCTURES. THE BEST AND THE SECOND BEST PERFORMANCE IS MARKED BY **BOLD** AND UNDERLINED, RESPECTIVELY.

Methods	<i>AG</i>	<i>EN</i>	<i>SD</i>	<i>SF</i>	<i>VIFF</i>	<i>Q<sub>abf</sub></i>
w/o DIIM	4.4747	6.9185	9.4503	0.0422	<b>0.9755</b>	0.4105
w/o ACIIM	5.3814	<u>7.1582</u>	<u>10.2160</u>	0.0545	0.8026	<u>0.6123</u>
Ours	<b>5.6864</b>	<b>7.2355</b>	<b>10.2413</b>	<b>0.0572</b>	<u>0.8374</u>	<b>0.6295</b>

Table III provides an objective comparison of our ATFuse with another two network structures. Apparently, our method can achieve the best performance in *AG*, *EN*, *SD*, *SF*, *Q<sub>abf</sub>*, and the second-best performance in *VIFF*. Therefore, the proposed DIIM and ACIIM can fully extract useful features, which enhance the retention of discrepancy information and the injection of common information in the fusion results, respectively.

2) *Ablation Study on Pixel Loss Function*: To identify the impact of the segmented pixel loss function, we conduct four experiments by using different pixel loss functions  $\mathcal{L}_1$  ( $\alpha = 100$ ),  $\mathcal{L}_2$  ( $\alpha = 0$ ),  $\mathcal{L}_3$  ( $\alpha = 50$ ) and  $\mathcal{L}_4$  ( $\alpha = 80$ ) in Eq. (16). Actually,  $\mathcal{L}_1$  and  $\mathcal{L}_2$  correspond to pixel maximum constraint and average constraint, respectively. Fig. 10 shows the fusion outcomes of two image pairs with the five different loss functions. From the red boxes in Fig. 10 (c, e, f), it can be obviously seen that the results generated by using  $\mathcal{L}_1$ ,  $\mathcal{L}_3$  and  $\mathcal{L}_4$  have different degrees of detail loss. Besides, as the value of  $\alpha$  increases, the degree of detail loss becomes serious. It is because of the increasing value of  $\alpha$ , more pixels in the image are constrained by the maximum value selection loss, which leads to some necessary information loss from one of the source images in fusion results. The results obtained by the  $\mathcal{L}_2$  loss lack brightness information than the results of other loss functions (see the green box in Fig. 10(d)), this is because the essence of  $\mathcal{L}_2$  loss is pixel average constraint. On the whole, setting  $\alpha$  to 20 results in a satisfactory trade-off between maintaining detail and preserving saliency.

Table IV presents the objective comparison of our ATFuse approach integrated with various loss functions. The average outcomes of six objective evaluation metrics are tabulated in Table IV. The best and second-best results for each metric are bolded and underlined, respectively. It can be seen results



Fig. 9. Fusion results obtained by three different network structures. (a) infrared image, (b) visible image, (c) the results of w/o DIIM, (d) the results of w/o ACIIM, (e) Ours.

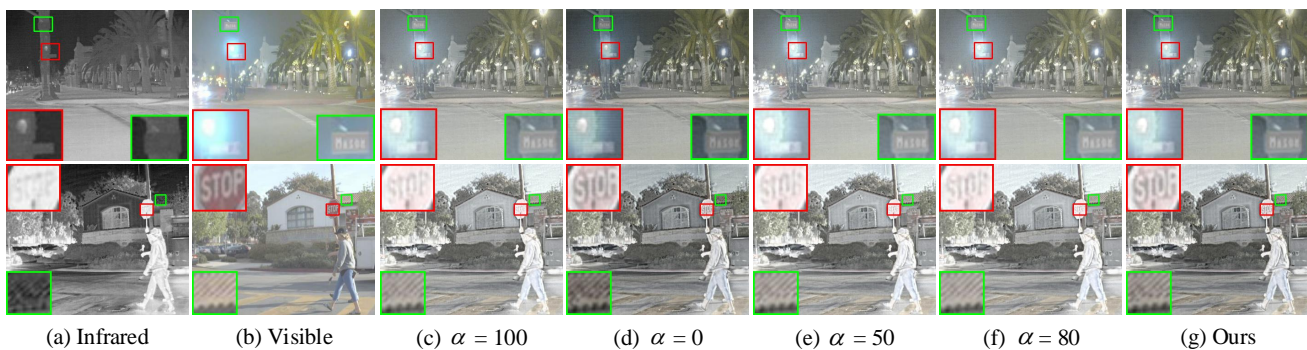


Fig. 10. Fusion results obtained by the proposed method with five different pixel loss functions. (a) infrared image, (b) visible image, (c) the results of  $\mathcal{L}_1$ , (d) the results of  $\mathcal{L}_2$ , (e) the results of  $\mathcal{L}_3$ , (f) the results of  $\mathcal{L}_4$ , (g) Ours.

TABLE IV

QUANTITATIVE COMPARISON OF FUSION RESULTS OBTAINED BY THE PROPOSED METHOD WITH FIVE DIFFERENT PIXEL LOSS FUNCTIONS. THE BEST AND THE SECOND BEST PERFORMANCE IS MARKED BY **BOLD** AND UNDERLINED, RESPECTIVELY.

Loss Functions	<i>AG</i>	<i>EN</i>	<i>SD</i>	<i>SF</i>	<i>VIFF</i>	<i>Q<sub>abf</sub></i>
$\mathcal{L}_1$ ( $\alpha = 100$ )	5.4194	7.1378	10.1297	0.0546	0.8298	0.5913
$\mathcal{L}_2$ ( $\alpha = 0$ )	<b>5.7090</b>	7.1636	9.9904	<b>0.0633</b>	0.7897	<u>0.6233</u>
$\mathcal{L}_3$ ( $\alpha = 50$ )	5.5444	<u>7.1843</u>	<b>10.2633</b>	0.0556	0.8281	0.6038
$\mathcal{L}_4$ ( $\alpha = 80$ )	5.4129	7.1334	10.1725	0.0549	<b>0.8391</b>	0.6071
Ours ( $\alpha = 20$ )	<u>5.6864</u>	<b>7.2355</b>	<u>10.2413</u>	<u>0.0572</u>	<u>0.8374</u>	<b>0.6295</b>

TABLE V

QUANTITATIVE COMPARISON OF FUSION RESULTS OBTAINED BY DIFFERENT  $\gamma$  VALUES. THE BEST AND THE SECOND BEST PERFORMANCE IS MARKED BY **BOLD** AND UNDERLINED, RESPECTIVELY.

Hyperparameter	<i>AG</i>	<i>EN</i>	<i>SD</i>	<i>SF</i>	<i>VIFF</i>	<i>Q<sub>abf</sub></i>
$\gamma = 0.5$	5.3458	<u>7.1918</u>	<u>10.2105</u>	0.0528	0.8091	0.5727
$\gamma = 0.75$	<u>5.4344</u>	7.1711	10.2065	<u>0.0552</u>	0.8286	<u>0.6212</u>
$\gamma = 1.0$	<b>5.6864</b>	<b>7.2355</b>	<b>10.2413</b>	<b>0.0572</b>	<b>0.8374</b>	<b>0.6295</b>

generated by our method outperform those of other loss functions in terms of most objective evaluations. Therefore, the choice of  $\alpha$  to 20 is reasonable in our study.

### E. Analysis of Some Configurations

1) *Hyperparameter  $\gamma$* : As mentioned in Section III-C, the hyperparameter  $\gamma$  controls the weight of pixel loss and texture loss in the loss function. Based on our experience, we set  $\gamma$  to 0.5, 0.75, and 1.0. Fig. 11 displays the fusion images produced by ATFuse using different  $\gamma$  values in the loss function. It can be seen that the output obtained with  $\gamma = 1.0$  exhibits

clear texture details around the windows. Table V presents an objective comparison of ATFuse using different  $\gamma$  values. It is evident from the Table that setting  $\gamma$  to 1.0 yields the best objective performance.

2) *Number of Feature Fusion Modules*: We assembled one DIIM and two ACIIMs into a single feature fusion module, as shown in Fig. 1 The number of feature fusion modules can be decided by inspecting the fusion performance through objective metrics. Table VI reports the quantitative fusion results by using various number of feature fusion modules. It can be seen that using one feature fusion module in the proposed framework achieves the best overall effect. Therefore, considering computational efficiency, one group of modules is



Fig. 11. Fusion results obtained by the proposed method with different  $\gamma$  values. (a) infrared image, (b) visible image, (c-e) the qualitative results of different  $\gamma$ .

TABLE VI

QUANTITATIVE COMPARISON OF FUSION RESULTS OBTAINED BY THE PROPOSED METHOD WITH DIFFERENT NUMBER OF FEATURE FUSION MODULES. THE BEST AND THE SECOND BEST PERFORMANCE IS MARKED BY **BOLD** AND UNDERLINED, RESPECTIVELY.

Number	$AG$	$EN$	$SD$	$SF$	$VIFF$	$Q_{abf}$
Three	<u>5.6557</u>	<b>7.2357</b>	<u>10.2076</u>	0.0570	0.8431	<u>0.6229</u>
Two	5.4366	7.1983	10.1812	0.0558	<b>0.8538</b>	0.6215
One (Ours)	<b>5.6864</b>	<u>7.2355</u>	<b>10.2413</b>	<b>0.0572</b>	0.8374	<b>0.6295</b>

suitable to fuse features.

### F. Computational Efficiency

The average computation time of seven different fusion methods across four IV datasets is listed in Table VII. The most efficient and second most efficient methods in each dataset are highlighted in bold and underlined, respectively. It can be seen that U2Fusion performs the highest efficiency while our method and DenseFuse both rank second. This is because our ATFuse method consumes time to alternately extract common information. Among all fusion methods, it is apparent that our ATFuse is powerful and relatively lightweight in terms of fusion performance and running speed over others.

## V. CONCLUSION

In this article, we observed that using the cross-attention mechanism directly for multimodal image fusion only extracted common information between source images, while ignoring the extraction of discrepancy information. Therefore, we modified cross-attention and proposed DIIM to extract discrepancy information from two modality images. Additionally, to mine and integrate long dependencies, we designed an alternate common information injection module (ACIIM) based on the vanilla cross-attention structure. Based on these two modules, we developed a novel IV-IF network named ATFuse. Specifically, we first applied the DIIM module to extract discrepancy information between source images, and then

alternately extracted common information. To realize a good balance between salient information and detail information retention, we proposed a segmented pixel loss function, which utilized different constraint conditions for diverse pixel parts according to the importance of pixels. The proposed method has been validated for its effectiveness on the RoadScene and MSRS datasets. Furthermore, we applied this method to other IV datasets, indicating that our method has excellent generalization ability. In comparison with six state-of-the-art fusion methods, extensive experiments show that ATFuse achieves the best fusion efficiency in both evaluations and computation burden.

## REFERENCES

- [1] Perushan Rajah, John Odindi, and Onesimo Mutanga. Feature level image fusion of optical imagery and synthetic aperture radar (sar) for invasive alien plant species detection and mapping. *Remote Sensing Applications: Society and Environment*, 10:198–208, 2018.
- [2] Qiang Zhang, Tonglin Xiao, Nianchang Huang, Dingwen Zhang, and Jungong Han. Revisiting feature fusion for rgb-t salient object detection. *IEEE Transactions on Circuits and Systems for Video Technology*, 31(5):1804–1818, 2020.
- [3] Qian Chen, Keren Fu, Ze Liu, Geng Chen, Hongwei Du, Bensheng Qiu, and Ling Shao. Ef-net: A novel enhancement and fusion network for rgb-d saliency detection. *Pattern Recognition*, 112:107740, 2021.
- [4] Ming Yin, Xiaoning Liu, Yu Liu, and Xun Chen. Medical image fusion with parameter-adaptive pulse coupled neural network in nonsubsampling shearlet transform domain. *IEEE Transactions on Instrumentation and Measurement*, 68(1):49–64, 2018.
- [5] Jing Yuan, Huan Chen, Fengchi Sun, and Yalou Huang. Multisensor information fusion for people tracking with a mobile robot: A particle filtering approach. *IEEE transactions on Instrumentation and Measurement*, 64(9):2427–2442, 2015.
- [6] Jiayi Ma, Yong Ma, and Chang Li. Infrared and visible image fusion methods and applications: A survey. *Information Fusion*, 45:153–178, 2019.
- [7] Yu Liu, Xun Chen, Zengfu Wang, Z Jane Wang, Rabab K Ward, and Xuesong Wang. Deep learning for pixel-level image fusion: Recent advances and future prospects. *Information Fusion*, 42:158–173, 2018.
- [8] Hui Li, Xiao-Jun Wu, and Josef Kittler. Mdlatlr: A novel decomposition method for infrared and visible image fusion. *IEEE Transactions on Image Processing*, 29:4733–4746, 2020.
- [9] Jiao Mou, Wei Gao, and Zongxi Song. Image fusion based on non-negative matrix factorization and infrared feature extraction. In *2013 6th International Congress on Image and Signal Processing (CISP)*, volume 2, pages 1046–1050. IEEE, 2013.

TABLE VII

AVERAGE RUNNING TIME OF ONE IMAGE PAIR ON FOUR DIFFERENT DATASETS BY USING DIFFERENT FUSION METHODS (UNIT: SECOND). THE BEST AND THE SECOND BEST PERFORMANCE IS MARKED BY **BOLD** AND UNDERLINED, RESPECTIVELY.

Datasets	DATFuse	DenseFuse	FusionGAN	RFN-Nest	SwinFusion	U2Fusion	Ours
TNO (s)	0.1354	0.1066	0.2382	0.1781	1.6576	<b>0.0675</b>	<u>0.1026</u>
RoadScene (s)	0.1248	0.1082	0.3129	0.1515	0.9637	<b>0.0682</b>	<u>0.1081</u>
MSRS (s)	0.1419	<u>0.1033</u>	0.1401	0.1832	1.7043	<b>0.0691</b>	0.1054

- [10] Durga Prasad Bavirisetti and Ravindra Dhuli. Two-scale image fusion of visible and infrared images using saliency detection. *Infrared Physics & Technology*, 76:52–64, 2016.
- [11] Lihua Jian, Rakiba Rayhana, Ling Ma, Shaowu Wu, Zheng Liu, and Huiqin Jiang. Infrared and visible image fusion based on deep decomposition network and saliency analysis. *IEEE Transactions on Multimedia*, 24:3314–3326, 2021.
- [12] Dong Yu, Suzhen Lin, Xiaofei Lu, Bin Wang, Dawei Li, and Yanbo Wang. A multi-band image synchronous fusion method based on saliency. *Infrared Physics & Technology*, 127:104466, 2022.
- [13] Jiayi Ma, Chen Chen, Chang Li, and Jun Huang. Infrared and visible image fusion via gradient transfer and total variation minimization. *Information Fusion*, 31:100–109, 2016.
- [14] Ramachandra Raghavendra, Bernadette Dorizzi, Ashok Rao, and G Hemantha Kumar. Particle swarm optimization based fusion of near infrared and visible images for improved face verification. *Pattern Recognition*, 44(2):401–411, 2011.
- [15] Ruichao Hou, Rencan Nie, Dongming Zhou, Jinde Cao, and Dong Liu. Infrared and visible images fusion using visual saliency and optimized spiking cortical model in non-subsampled shearlet transform domain. *Multimedia Tools and Applications*, 78:28609–28632, 2019.
- [16] Jiacheng Ying, Can Tong, Zehua Sheng, Bowen Yao, Si-Yuan Cao, Heng Yu, and Hui-Liang Shen. Region-aware rgb and near-infrared image fusion. *Pattern Recognition*, page 109717, 2023.
- [17] Hui Li and Xiao-Jun Wu. Densefuse: A fusion approach to infrared and visible images. *IEEE Transactions on Image Processing*, 28(5):2614–2623, 2018.
- [18] Hui Li, Xiao-Jun Wu, and Josef Kittler. Rfn-nest: An end-to-end residual fusion network for infrared and visible images. *Information Fusion*, 73:72–86, 2021.
- [19] Lihua Jian, Xiaomin Yang, Zheng Liu, Gwanggil Jeon, Mingliang Gao, and David Chisholm. Sedrfuse: A symmetric encoder–decoder with residual block network for infrared and visible image fusion. *IEEE Transactions on Instrumentation and Measurement*, 70:1–15, 2020.
- [20] Meilong Xu, Linfeng Tang, Hao Zhang, and Jiayi Ma. Infrared and visible image fusion via parallel scene and texture learning. *Pattern Recognition*, 132:108929, 2022.
- [21] Siling Feng, Can Wu, Cong Lin, and Mengxing Huang. Radfnnet: An infrared and visible image fusion framework based on distributed network. *Frontiers in Plant Science*, 13, 2022.
- [22] Dong Liu, Huihua Yang, and Yuying Shao. Fusion of infrared and visible light images for object detection based on cnn. In *2021 10th International Conference on Internet Computing for Science and Engineering*, pages 110–115. 2021.
- [23] Le Sun, Yuhang Li, Min Zheng, Zhaoyi Zhong, and Yanchun Zhang. Mcnnet: Multiscale visible image and infrared image fusion network. *Signal Processing*, 208:108996, 2023.
- [24] Han Xu, Jiayi Ma, Junjun Jiang, Xiaojie Guo, and Haibin Ling. U2fusion: A unified unsupervised image fusion network. *IEEE Transactions on Pattern Analysis and Machine Intelligence*, 44(1):502–518, 2020.
- [25] Jiayi Ma, Wei Yu, Pengwei Liang, Chang Li, and Junjun Jiang. Fusion-gan: A generative adversarial network for infrared and visible image fusion. *Information fusion*, 48:11–26, 2019.
- [26] Hongzhi Zhang, Yifan Shen, Yangyan Ou, Bo Ji, and Jia He. A gan-based visible and infrared image fusion algorithm. In *AOPC 2021: Infrared Device and Infrared Technology*, volume 12061, pages 215–221. SPIE, 2021.
- [27] Jing Li, Hongtao Huo, Kejian Liu, and Chang Li. Infrared and visible image fusion using dual discriminators generative adversarial networks with wasserstein distance. *Information Sciences*, 529:28–41, 2020.
- [28] Jiangtao Xu, Xingping Shi, Shuzhen Qin, Kaige Lu, Han Wang, and Jianguo Ma. Lbp-began: A generative adversarial network architecture for infrared and visible image fusion. *Infrared Physics & Technology*, 104:103144, 2020.
- [29] Ashish Vaswani, Noam Shazeer, Niki Parmar, Jakob Uszkoreit, Llion Jones, Aidan N Gomez, Łukasz Kaiser, and Illia Polosukhin. Attention is all you need. *Advances in neural information processing systems*, 30, 2017.
- [30] Chengjun Li, Xinhao Wu, and Youyu Wu. Research and implementation of transformer label detection algorithm based on machine vision. In *IOP Conference Series: Materials Science and Engineering*, volume 782, page 032032. IOP Publishing, 2020.
- [31] Anjith George and Sébastien Marcel. On the effectiveness of vision transformers for zero-shot face anti-spoofing. In *2021 IEEE International Joint Conference on Biometrics (IJCB)*, pages 1–8. IEEE, 2021.
- [32] Xiangning Chen, Cho-Jui Hsieh, and Boqing Gong. When vision transformers outperform resnets without pre-training or strong data augmentations. *arXiv preprint arXiv:2106.01548*, 2021.
- [33] Tengfei You, Chanyue Wu, Yunpeng Bai, Dong Wang, Huibin Ge, and Ying Li. Hmf-former: Spatio-spectral transformer for hyperspectral and multispectral image fusion. *IEEE Geoscience and Remote Sensing Letters*, 2022.
- [34] Vibashan Vs, Jeya Maria Jose Valanarasu, Poojan Oza, and Vishal M Patel. Image fusion transformer. In *2022 IEEE International Conference on Image Processing (ICIP)*, pages 3566–3570. IEEE, 2022.
- [35] Jing Zhang, Aiping Liu, Dan Wang, Yu Liu, Z Jane Wang, and Xun Chen. Transformer-based end-to-end attention and functional image fusion. *IEEE Transactions on Instrumentation and Measurement*, 71:1–11, 2022.
- [36] Yu Yuan, Jiaqi Wu, Zhongliang Jing, Henry Leung, and Han Pan. Multimodal image fusion based on hybrid cnn-transformer and non-local cross-modal attention. *arXiv preprint arXiv:2210.09847*, 2022.
- [37] Wei Tang, Fazhi He, Yu Liu, Yansong Duan, and Tongzhen Si. Datfuse: Infrared and visible image fusion via dual attention transformer. *IEEE Transactions on Circuits and Systems for Video Technology*, 2023.
- [38] Xiaoling Zhou, Zetao Jiang, and Idowu Paul Okuwobi. Cafnet: Cross-attention fusion network for infrared and low illumination visible-light image. *Neural Processing Letters*, pages 1–15, 2022.
- [39] Jiayi Ma, Linfeng Tang, Fan Fan, Jun Huang, Xiaoguang Mei, and Yong Ma. Swinfusion: Cross-domain long-range learning for general image fusion via swin transformer. *IEEE/CAA Journal of Automatica Sinica*, 9(7):1200–1217, 2022.
- [40] Yuzhao Chen, Tao Dai, Xi Xiao, Jian Lu, and Shu-Tao Xia. Enhanced image restoration via supervised target feature transfer. In *2020 IEEE International Conference on Image Processing (ICIP)*, pages 1028–1032. IEEE, 2020.
- [41] Caihong Yuan, Chunyan Xu, Tianjiang Wang, Fang Liu, Zhiqiang Zhao, Ping Feng, and Jingjuan Guo. Deep multi-instance learning for end-to-end person re-identification. *Multimedia Tools and Applications*, 77:12437–12467, 2018.
- [42] Deqiang Ouyang, Jie Shao, Yonghui Zhang, Yang Yang, and Heng Tao Shen. Video-based person re-identification via self-paced learning and deep reinforcement learning framework. In *Proceedings of the 26th ACM international conference on Multimedia*, pages 1562–1570. 2018.
- [43] Yungang Zhang and Yu Xiang. Recent advances in deep learning for single image super-resolution. In *Advances in Brain Inspired Cognitive Systems: 9th International Conference, BICS 2018, Xi’an, China, July 7-8, 2018, Proceedings*, pages 85–95. Springer, 2018.
- [44] Yu Liu, Xun Chen, Juan Cheng, Hu Peng, and Zengfu Wang. Infrared and visible image fusion with convolutional neural networks. *International Journal of Wavelets, Multiresolution and Information Processing*, 16(03):1850018, 2018.
- [45] Jiayi Ma, Linfeng Tang, Meilong Xu, Hao Zhang, and Guobao Xiao. Stdffusionnet: An infrared and visible image fusion network based on salient target detection. *IEEE Transactions on Instrumentation and Measurement*, 70:1–13, 2021.
- [46] Qilei Li, Lu Lu, Zhen Li, Wei Wu, Zheng Liu, Gwanggil Jeon, and Xiaomin Yang. Coupled gan with relativistic discriminators for infrared

- and visible images fusion. *IEEE Sensors Journal*, 21(6):7458–7467, 2019.
- [47] Jiayi Ma, Han Xu, Junjun Jiang, Xiaoguang Mei, and Xiao-Ping Zhang. Ddcgan: A dual-discriminator conditional generative adversarial network for multi-resolution image fusion. *IEEE Transactions on Image Processing*, 29:4980–4995, 2020.
- [48] Jiayi Ma, Hao Zhang, Zhenfeng Shao, Pengwei Liang, and Han Xu. Ganmcc: A generative adversarial network with multiclassification constraints for infrared and visible image fusion. *IEEE Transactions on Instrumentation and Measurement*, 70:1–14, 2020.
- [49] Alexey Dosovitskiy, Lucas Beyer, Alexander Kolesnikov, Dirk Weisenseborn, Xiaohua Zhai, Thomas Unterthiner, Mostafa Dehghani, Matthias Minderer, Georg Heigold, Sylvain Gelly, et al. An image is worth 16x16 words: Transformers for image recognition at scale. *arXiv preprint arXiv:2010.11929*, 2020.
- [50] Tianming Xie, Zhonghao Zhang, Jing Tian, and Lihong Ma. Focal detr: Target-aware token design for transformer-based object detection. *Sensors*, 22(22):8686, 2022.
- [51] Jian Lin, Kai Zhang, Xi Yang, Xiangzheng Cheng, and Chenhui Li. Infrared dim and small target detection based on u-transformer. *Journal of Visual Communication and Image Representation*, 89:103684, 2022.
- [52] Zhizhong Xi, Jingen Wang, and Yanqing Kang. Oriented target detection algorithm based on transformer. In *2021 4th International Conference on Artificial Intelligence and Pattern Recognition*, pages 22–28. 2021.
- [53] Guanxiao Li, Ke Zhang, Yu Su, and Jingyu Wang. Feature pre-inpainting enhanced transformer for video inpainting. *Engineering Applications of Artificial Intelligence*, 123:106323, 2023.
- [54] Hongshan Gan and Yi Wan. A hybrid encoder transformer network for video inpainting. In *2022 2nd International Conference on Computer, Control and Robotics (ICCCR)*, pages 230–234. IEEE, 2022.
- [55] Gajanan Tudavekar, Santosh S Saraf, and Sanjay R Patil. Spatio-temporal inference transformer network for video inpainting. *International Journal of Image and Graphics*, page 2350007, 2021.
- [56] Beiji Zou, Zexin Ji, Chengzhang Zhu, Yulan Dai, Wensheng Zhang, and Xiaoyan Kui. Multi-scale deformable transformer for multi-contrast knee mri super-resolution. *Biomedical Signal Processing and Control*, 79:104154, 2023.
- [57] Guangwei Gao, Zixiang Xu, Juncheng Li, Jian Yang, Tiejong Zeng, and Guo-Jun Qi. Ctcnet: A cnn-transformer cooperation network for face image super-resolution. *IEEE Transactions on Image Processing*, 32:1978–1991, 2023.
- [58] Ido Ariav and Israel Cohen. Fully cross-attention transformer for guided depth super-resolution. *Sensors*, 23(5):2723, 2023.
- [59] Wei Tang, Fazhi He, and Yu Liu. Tccfusion: An infrared and visible image fusion method based on transformer and cross correlation. *Pattern Recognition*, 137:109295, 2023.
- [60] Zhihao Chang, Zhixi Feng, Shuyuan Yang, and Quanwei Gao. Aft: Adaptive fusion transformer for visible and infrared images. *IEEE Transactions on Image Processing*, 32:2077–2092, 2023.
- [61] Jun Chen, Jianfeng Ding, Yang Yu, and Wenping Gong. Thfuse: An infrared and visible image fusion network using transformer and hybrid feature extractor. *Neurocomputing*, 2023.
- [62] Kaixin Yu, Xiaoming Yang, Seunggil Jeon, and Qingyu Dou. An end-to-end medical image fusion network based on swin-transformer. *Microprocessors and Microsystems*, 98:104781, 2023.
- [63] Zhishe Wang, Yanlin Chen, Wenyu Shao, Hui Li, and Lei Zhang. Swin-fuse: A residual swin transformer fusion network for infrared and visible images. *IEEE Transactions on Instrumentation and Measurement*, 71:1–12, 2022.
- [64] Tete Xiao, Mannat Singh, Eric Mintun, Trevor Darrell, Piotr Dollár, and Ross Girshick. Early convolutions help transformers see better. *Advances in Neural Information Processing Systems*, 34:30392–30400, 2021.
- [65] Linfeng Tang, Jiteng Yuan, Hao Zhang, Xingyu Jiang, and Jiayi Ma. Piafusion: A progressive infrared and visible image fusion network based on illumination aware. *Information Fusion*, 83:79–92, 2022.
- [66] Yu Liu, Shuping Liu, and Zengfu Wang. A general framework for image fusion based on multi-scale transform and sparse representation. *Information fusion*, 24:147–164, 2015.
- [67] Yun-Jiang Rao. In-fibre bragg grating sensors. *Measurement science and technology*, 8(4):355, 1997.
- [68] Yufeng Zheng, Edward A Essock, Bruce C Hansen, and Andrew M Haun. A new metric based on extended spatial frequency and its application to dwt based fusion algorithms. *Information Fusion*, 8(2):177–192, 2007.
- [69] Yu Han, Yunze Cai, Yin Cao, and Xiaoming Xu. A new image fusion performance metric based on visual information fidelity. *Information fusion*, 14(2):127–135, 2013.